

# ADAPTIVE SEA LION OPTIMIZED RESNET50 (SLIA-RN50) FOR ENHANCED MRI TUMOR CLASSIFICATION

S. SHANMUGAPRIYA<sup>1</sup>, P. RUTRAVIGNESHWARAN<sup>2</sup>

<sup>1</sup>PhD Research Scholar, Department of Computer Science, Karpagam Academy of Higher Education, Coimbatore, Tamil Nadu, India.

and Assistant Professor, Department of Computer Science and Data Science, Nehru Arts and Science College, Coimbatore, Tamil Nadu, India.

<sup>2</sup>Assistant Professor, Department of Computer Science, Karpagam Academy of Higher Education, Coimbatore, Tamil Nadu, India.

<sup>1</sup>sspriya818@gmail.com, <sup>2</sup>rutra20190@gmail.com

## ABSTRACT

MRI-based tumor classification requires high precision, adaptability, and computational efficiency to ensure reliable diagnosis. Conventional deep learning models struggle with feature extraction, misclassification, and optimization inefficiencies, limiting their effectiveness in medical imaging. The purpose of this study is to enhance classification performance by integrating bio-inspired optimization with deep learning. A Sea Lion Inspired Adaptive ResNet50 (SLIA-RN50) framework is introduced to optimize hierarchical feature extraction, improve adaptability, and enhance decision-making in MRI tumor classification. The methodology involves leveraging sea lion-inspired strategies to refine multi-scale integration, collaborative filtering, and energy-efficient processing, ensuring balanced precision and recall. The proposed SLIA-RN50 model outperforms existing architectures in classification accuracy, precision, and F-measure, significantly reducing false positives and false negatives. Experimental results validate the effectiveness of the optimized framework, confirming its potential for automated MRI-based tumor detection. The bio-inspired model presents an efficient and scalable solution for improving computational techniques in medical image classification.

**Keywords:** *MRI Tumor Classification - ResNet50 - Sea Lion Optimization - Medical Image Processing - Feature Extraction*

## 1. INTRODUCTION

Brain tumors are irregular cell growths in the brain, either benign or cancerous. Brain tumors greatly interfere with the brain's proper function, impacting different areas of health depending on their size, location, and rate of growth. Brain tumors can be caused by new tumor growth in the brain (primary tumors) or due to metastasis from other areas of the body (secondary or metastatic tumors) [1]. They pose a major health risk, resulting in cognitive problems, neurological impairments, and, in extreme situations, potentially fatal consequences.

The impact of brain tumors on individuals extends beyond physical health, often influencing mental and emotional well-being. Depending on their location, brain tumors can affect motor skills, speech, vision, and coordination [2]. Emotional and psychological effects such as anxiety, depression, and mood swings frequently occur due to both the tumor itself and the side effects of treatments. Brain tumors may also cause cognitive dysfunctions, including memory loss and difficulty in concentrating. Additionally, seizures are a common

symptom that arises from the tumor's disruption of the electrical activity in the brain. As the illness worsens, overall quality of life declines, therefore early identification and treatments are essential [3].

Machine learning and deep learning methodologies have revolutionized the field of brain tumor classification and prediction. These advanced computational techniques provide powerful tools for analyzing complex and high-dimensional data, significantly enhancing diagnostic and predictive accuracy [4]. Machine learning methodologies such as support vector machines, decision trees, and random forests analyze patterns within data to facilitate tumor diagnosis and predict tumor behavior. These algorithms undergo training on labeled datasets to recognize distinct features that differentiate various brain tumor types [5].

“Deep Learning”, a specialized branch of “Machine Learning” employs neural networks to achieve superior performance in processing and interpreting medical imaging data [6].

“Convolutional Neural Networks” (CNNs), a widely adopted deep learning architecture, demonstrate exceptional efficacy in analyzing MRI and CT scan images. These networks extract hierarchical features from images, enabling the detection and classification of tumors with remarkable precision [7]. The use of deep learning minimizes human error and reduces the time required for manual analysis, making it an indispensable asset in medical diagnostics. Machine learning and deep learning techniques also contribute to personalized treatment planning by predicting tumor growth patterns and treatment responses [8]. These methods analyze large datasets encompassing patient demographics, imaging results, genetic profiles, and treatment histories to create tailored therapeutic strategies. By identifying correlations and trends within the data, machine learning algorithms assist clinicians in selecting the most effective treatment modalities for individual patients [9]. Incorporating artificial intelligence into brain tumor research has led to significant advancements in early detection. Machine learning models can analyze subtle changes in imaging data, identifying potential tumors before symptoms manifest. This early detection capability enhances the chances of successful treatment and improves survival rates. AI-driven systems have the capability to integrate diverse data sources, including imaging, genomics, and clinical records, to generate comprehensive diagnostic insights. This multifaceted approach enhances the accuracy and reliability of tumor classification and assessment [10].

Brain tumor classification using MRI imaging has gained significant attention within deep learning-based medical imaging applications. MRI scans offer high-resolution, non-invasive visualization of brain structures, making them a preferred modality for detecting and evaluating tumors [11]. Deep learning models, especially CNNs, are widely used for segmenting and classifying MRI images. These models distinguish between tumor types, grades, and subregions with exceptional accuracy. MRI-based classification involves several steps, including image preprocessing, feature extraction, and classification [12]. Preprocessing enhances the quality of images by reducing noise and standardizing intensity values. Feature extraction captures essential characteristics of the tumor, such as shape, size, and texture, which are crucial for accurate classification. Finally, classification algorithms categorize the tumor based on the extracted features, aiding in diagnosis and treatment planning [13]. The integration of advanced

computational techniques with MRI imaging has led to the development of automated systems for brain tumor classification. These systems reduce the dependency on manual interpretation, providing consistent and reliable results. Automated classification systems are especially valuable in clinical settings, where radiologists face time constraints and a high volume of imaging data [14].

MRI-based deep learning models have demonstrated high sensitivity and specificity in detecting tumors, including small or early-stage growths that may be overlooked during manual analysis. These models can differentiate between tumor grades, such as low-grade and high-grade gliomas, aiding in treatment decision-making [15]. The ability of deep learning to accurately assess tumor boundaries and volumes further supports surgical planning and post-treatment monitoring. The combination of machine learning, deep learning, and MRI imaging has transformed the landscape of brain tumor research and clinical practice [16]. By enabling precise classification and prediction, these technologies contribute to improved diagnostic accuracy, personalized treatments, and better patient outcomes. The integration of these advancements into routine clinical workflows has the potential to significantly enhance the management of brain tumors, ultimately saving lives and improving quality of life for affected individuals [5].

ResNet50 is a “Deep Convolutional Neural Network” renowned for its remarkable performance in image classification tasks. Designed with 50 layers, ResNet50 leverages residual learning to address the problem of vanishing gradients in deep networks, ensuring efficient training and high accuracy [17]. The architecture consists of convolutional layers, batch normalization, ReLU activations, and identity connections, allowing the model to preserve essential features across layers. In MRI classification, ResNet50 has been extensively used because it can extract complex features from high-dimensional medical images. Transfer learning often enhances performance in medical applications by fine-tuning a pre-trained ResNet50 model on specific MRI datasets [17].

ResNet50's residual connections allow the network to maintain performance even with increasing depth, ensuring effective feature propagation. This capability is critical for accurately classifying complex medical images, including detecting and grading brain tumors. By integrating advanced feature extraction and robust classification

capabilities, ResNet50 has become a reliable tool for automating MRI image analysis, reducing diagnostic time and improving accuracy in clinical decision-making. Its application supports precise tumor identification, aiding in early diagnosis and treatment planning [18].

Bio-inspired computing leverages nature-inspired algorithms to optimize machine learning (ML) and deep learning (DL) models by enhancing adaptability, efficiency, and accuracy [19]. Drawing inspiration from biological processes such as swarm intelligence, evolutionary strategies, and neural adaptability, bio-inspired optimization fine-tunes hyperparameters, improves feature selection, and enhances convergence speed in ML and DL architectures. Techniques like particle swarm optimization, genetic algorithms, and ant colony optimization dynamically optimize model performance while reducing computational complexity [20], [38]-[70].

This study focuses on developing MRI-based brain tumor classification through bio-inspired optimization by implementing adaptive mechanisms inspired by sea lion attributes into ResNet50 architecture. The method aims to enhance feature recognition while making learning more efficient while lowering classification errors between different tumor types. The research relies on a MRI dataset that contains diverse tumor characteristics, imaging conditions for ensuring the model achieves broad generalization across various cases. The performance of this model might be affected by unbalanced dataset content and imaging defects as well as rare tumor morphologies. Further applications will need parameter adjustments for particular clinical databases and actual clinical environments since the main analysis utilized a dataset with established imaging constraints.

### 1.1. Problem Statement

Traditional ML and DL models often struggle with computational inefficiency, suboptimal feature extraction, and lack of adaptability when applied to complex medical imaging tasks such as MRI-based brain tumor classification. Conventional optimization techniques frequently lead to local minima, slow convergence, and inefficient resource utilization, limiting the models' robustness in handling variations in MRI scans. Natural intelligence-based bio-inspired optimization overcomes these obstacles by offering improved feature selection, self-adaptive learning, and energy-efficient calculations. Existing

architectures lack dynamic adaptability and multi-scale feature integration, reducing classification precision. The recent ParMamba [21] framework achieves better classification results using parallel CNN-Mamba architectures that maintain obstacles in adapting to new tasks and achieving high energy efficiency and biological learning processes. Efficient tumor classification on a large scale needs an architectural solution which recreates natural cognitive behavior.

### 1.2. Objective and Motivation

Medical image classification, particularly MRI-based tumor detection, demands high precision, adaptability, and computational efficiency. Conventional deep learning models often struggle with suboptimal feature extraction, inefficient parameter tuning, and slow convergence, affecting classification accuracy. The objective of this work is to develop an optimized framework inspired by the adaptive behavior of sea lions, ensuring hierarchical feature extraction, real-time adaptability, and energy-efficient processing in MRI classification. By integrating bio-inspired principles, this approach enhances model generalization, reduces computational overhead, and improves classification robustness. The motivation behind this work stems from the limitations of conventional optimization techniques, which frequently lead to overfitting, poor convergence, and excessive resource consumption. Sea lions exhibit dynamic decision-making, precise energy management, and multi-scale sensory processing, making them an ideal inspiration for optimizing ML and DL architectures. Implementing these adaptive strategies enables faster learning, improved feature selection, and enhanced classification accuracy in medical imaging. This work seeks to bridge the gap between biological intelligence and computational models, ensuring an effective and resource-efficient MRI classification framework.

The researchers seek to develop an adaptive version of ResNet50 through analysis of sea lion behavioral patterns with the goal of building better MRI tumor classifiers. The proposed model brings together innovative elements that unite dynamic learning functions with energy-conscious computations along with multi-scale features extraction. The model's performance validation is based on outcome measures that assess classification accuracy and F-measure along with FMI and MCC and precision and recall. SLIA-RN50 brings unique biological adaptiveness different from traditional deep learning approaches which results in high

diagnostic and computational performance for medical imaging analysis. The research pursues three main objectives which include improved classification depth through refined residual learning as well as feature redundancy reduction through collaborative filtering and enhanced training-based regional attention. The platform uses structural improvements to maintain performance stability and practical implementation capabilities for processing varied complex tumor database information.

## 2. LITERATURE REVIEW

“Cross-Fusion Segmenter” [21] introduced a unique multi-modal approach for brain tumor segmentation. The design has focused on modality-specific feature extraction using separate encoder paths, which have captured unique attributes from multiple imaging modalities. Cross-connection layers have ensured interaction between modalities, promoting shared learning while preserving individual characteristics. An attentional feature fusion mechanism has combined these insights, highlighting the most critical features for segmentation. “Explainable Glioma Classifier” [22] has developed a lightweight CNN model for classifying brain tumors with transparency. The model has emphasized simplicity and efficiency, reducing computational requirements while retaining high accuracy. Feature extraction layers have focused on capturing tumor-specific patterns with minimal complexity. The integration of explainable AI techniques has visualized the decision-making process, offering insights into model predictions. “Orthogonal Feature Enhancer” [23] introduces a novel framework that combines “Proper Orthogonal Decomposition (POD)” with deep learning networks for precise brain tumor detection. The approach has extracted essential features from MRI scans using POD, reducing dimensionality and noise while retaining critical data. The extracted features have been processed through a customized deep learning model for classification and detection.

“Neural Tumor Identifier” [24] introduced BrainNet, a deep learning framework designed for brain tumor classification. The model architecture has included multiple convolutional layers optimized for recognizing complex tumor features in MRI scans. Advanced pooling strategies have ensured retention of spatial information critical for accurate classification. “Weighted Fusion Classifier” [25] proposed a deep learning-based approach for brain tumor categorization on

imbalanced datasets. The design employed a weighted loss function to mitigate the impact of class imbalance, ensuring fair representation of all tumor types. Feature extraction has combined convolutional layers with a fusion mechanism to integrate high-level and low-level attributes. “DBN-Quadratic Boost” [26] introduced an advanced hybrid framework for brain tumor detection by integrating a “Deep Belief Network” (DBN) with a quadratic logit boost classifier. DBN has been employed to extract hierarchical and meaningful features from “Magnetic Resonance Images” (MRIs). The preprocessing phase has enhanced image quality by removing noise and adjusting contrast, ensuring optimal input for feature extraction.

“Boosted Tumor Detector” [27] has implemented a refined ensemble boosting strategy to enhance brain tumor detection accuracy. The model has combined weak classifiers into a robust ensemble capable of addressing complex tumor features. Preprocessing steps have included artifact removal and contrast optimization to prepare high-quality MRI images. “Fractal Feature Detector” [28] employed a multi-scale fractal feature network combined with fractal residual learning to enhance brain tumor detection. The method has extracted self-similar fractal patterns at varying scales, enabling a detailed analysis of both large and minute tumor regions. Residual learning has been incorporated to preserve critical information and mitigate feature loss during processing. Image preprocessing has included normalization and artifact removal to standardize MRI inputs.

“Dual Fusion Classifier” [29] presented DEF-SwinE2NET, combining dual feature enhancement with multi-model fusion for brain tumor classification. The preprocessing stage has refined MRI images through noise reduction and contrast optimization. The SwinE2NET architecture has integrated diverse deep learning models, extracting features that highlight key tumor-specific attributes. Dual enhancement techniques have amplified significant patterns, improving the classifier's ability to distinguish between tumor types. “Adaptive ResUNet Enhancer” [30] introduced a multiscale Atrous convolution-based ResUNet3+ for brain tumor segmentation and classification. Atrous convolutions have been utilized to capture features at various resolutions, ensuring accurate segmentation of intricate tumor regions. The model has incorporated attention-based

ensemble convolution networks to enhance feature focus, prioritizing tumor-specific patterns.

“Moth-Optimized Tumor Finder” [31] has integrated CNN segmentation with the “Moth-Flame Optimization Algorithm” (MFOA) for automatic brain tumor classification. The method employed CNN-based segmentation to isolate tumor regions from MRI images, ensuring precise boundaries and minimal noise interference. Feature extraction has combined deep learning and handcrafted techniques to capture both high-level and domain-specific attributes. “Lightweight Attention Segmenter” [32] introduced LATUP-Net, a compact 3D attention U-Net with parallel convolutions designed for efficient brain tumor segmentation. Parallel convolutional layers have processed features simultaneously, enhancing efficiency and reducing computation time. Attention mechanisms have focused on regions of interest, ensuring precise tumor segmentation. “Deep MRI Classifier” [33] proposed an advanced deep learning approach for brain tumor classification using MRI data. The framework employed a convolutional architecture optimized for extracting tumor-specific features. Image preprocessing has addressed quality inconsistencies, enhancing the clarity of input data.

“Disentangled Segmentation” [34] has implemented disentangled representation learning to separate shared and modality-specific features for multi-modal brain tumor segmentation. By isolating shared features, the approach has enabled the network to capture common characteristics across all imaging modalities while preserving unique aspects of each modality. Region-aware contrastive learning has further enhanced segmentation by focusing on key tumor regions, maximizing the network’s ability to differentiate between tumor and non-tumor areas. “FT-FEDTL Classifier” [35] has applied a transfer learning-based framework tailored for microwave-based brain tumor classification. By leveraging pre-trained models, the method has efficiently extracted domain-specific features relevant to tumor classification. Preprocessing has enhanced data quality by standardizing microwave signal inputs, ensuring consistent performance across diverse samples.

“PDCNN” [36] presents a “Parallel Deep Convolutional Neural Network” framework for detecting and classifying brain tumors in MRI scans. The model utilizes multiple CNN architectures running in parallel to extract diverse features from

medical images, improving classification accuracy. By leveraging deep feature representations, the approach distinguishes between tumor types and normal brain tissues effectively. The parallel structure enhances computational efficiency, allowing faster and more precise analysis. This method improves diagnostic accuracy and supports early detection, aiding clinicians in treatment planning. The integration of parallel networks ensures robust feature extraction and classification, making it a reliable solution for automated brain tumor analysis.

“ABT-DCNN” [37] introduces a “Deep Convolutional Neural Network” (DCNN)-based framework for accurate brain tumor detection in MRI images. The model extracts hierarchical features, enabling precise tumor localization and classification. Advanced deep learning techniques enhance pattern recognition, improving the distinction between healthy and tumor-affected regions. The CNN architecture efficiently processes high-resolution images, ensuring reliable diagnostic outcomes. The proposed system automates tumor detection, reducing manual intervention and increasing accuracy in clinical assessments.

### 3. SEA LION INSPIRED ADAPTIVE RESNET50 (SLIA-RESNET50)

Optimizing ResNet50 for MRI classification by incorporating the characteristics of sea lions involves drawing inspiration from their adaptive and efficient behaviors in hunting and navigation. Sea lions are known for their agility, energy conservation, and precise decision-making in complex environments. These traits can be translated into steps for enhancing ResNet50 performance.

#### 3.1. Efficient Preprocessing

Efficient preprocessing is a critical component of the SLIA-RN50 model, reflecting the sea lion’s behavior of efficiently focusing on relevant targets in complex aquatic environments. By mimicking the sea lion’s optimized sensory abilities, this step ensures that MRI images are processed to enhance the model’s accuracy and reliability. Optimized preprocessing aligns MRI data with SLIA-RN50’s requirements, emphasizing features critical for tumor classification while minimizing computational overhead. Fig 1. Depicts the overall framework of SLIA-RN50.

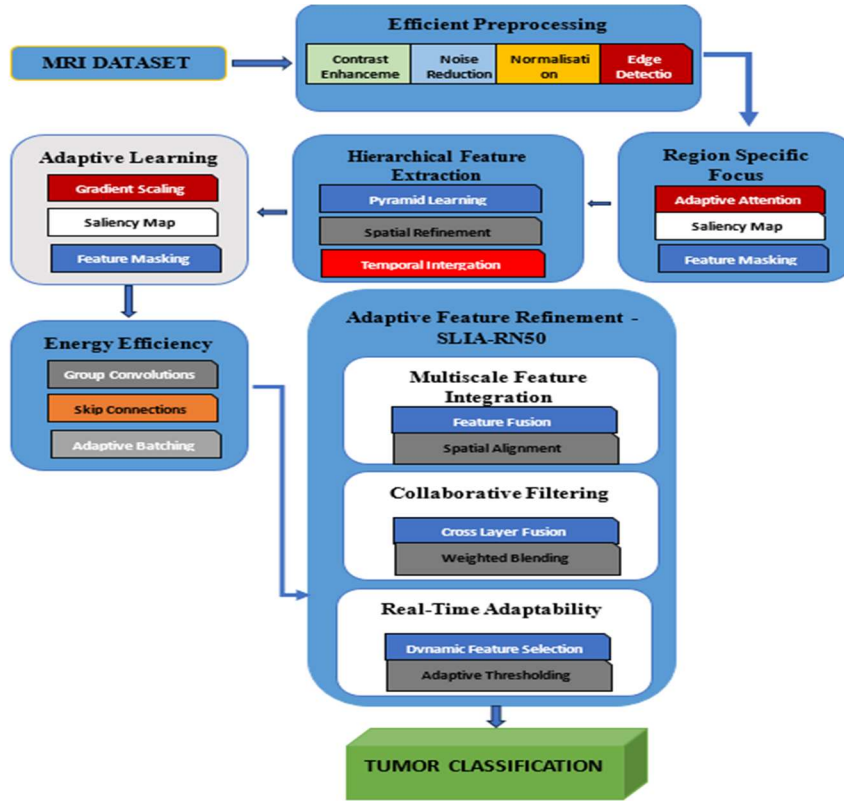


Fig 1. Architecture of SLIA-RN50

To emulate the sea lion's ability to discern fine details under varying light conditions, MRI images undergo contrast enhancement. This ensures that regions of interest, such as tumor boundaries, are highlighted. The contrast enhancement is achieved using the histogram equalization method which is expressed mathematically in Eq.(1).

$$p(x) = \frac{1}{MN} \sum_{i=0}^x h(i) \quad (1)$$

Where  $p(x)$  represents the probability distribution function for intensity levels,  $MN$  denotes the total number of pixels in the image, and  $h(i)$  is the frequency of intensity level  $i$ . The transformation stretches the contrast range, emphasizing areas critical for tumor detection. This aligns with the optimized behavior of sea lions, which adapt their vision to changing light underwater to focus on prey.

The removal of noise is crucial for the accurate classification of MRI images. Inspired by the sea lion's ability to filter irrelevant sensory inputs, noise reduction is applied using a Gaussian filter.

$$G(x, y) = \frac{1}{2\pi\sigma^2} e^{-\frac{x^2+y^2}{2\sigma^2}} \quad (2)$$

In Eq.(2), where  $G(x,y)$  represents the Gaussian kernel,  $\sigma$  denotes the standard deviation, and  $x, y$  are pixel coordinates. The Gaussian filter smoothens the image while preserving edges, ensuring that essential tumor features remain intact. This reflects the optimized focus of sea lions on relevant stimuli, minimizing distractions in their surroundings.

To maintain consistency across MRI datasets with varying intensity levels, intensity normalization is implemented. This step mirrors the sea lion's adaptability to environmental variability by standardizing input data for optimal processing. The normalization is achieved as represented mathematically in Eq.(3).

$$I'(x, y) = \frac{I(x, y) - \mu}{\sigma} \quad (3)$$

where  $I'(x,y)$  represents the normalized intensity,  $I(x,y)$  is the original intensity,  $\mu$  is the mean intensity, and  $\sigma$  is the standard deviation. Normalization ensures that all input images are brought to a common intensity scale, enhancing the robustness of feature extraction.

Sea lions optimize their movements to conserve energy by adapting to spatial constraints.

Similarly, MRI images are adaptively resampled to standardize their resolution while preserving critical spatial details. Adaptive resampling employs bilinear interpolation is clearly expressed in mathematical form in Eq.(4).

$$I_r(x, y) = \frac{1}{(x_2 - x_1)(y_2 - y_1)} \sum_{i=x_1}^{x_2} \sum_{j=y_1}^{y_2} I(i, j) \quad (4)$$

Where  $I_r(x, y)$  represents the resampled image at the coordinates  $(x, y)$ , and  $I(i, j)$  denotes the intensity of neighboring pixels within a bounding box defined by  $(x_1, y_1)$  and  $(x_2, y_2)$ . This method balances resolution optimization and computational efficiency, mirroring the sea lion's energy-conserving strategies.

Sea lions utilize optimized sensory mechanisms to detect prey outlines effectively. Similarly, edge detection highlights tumor boundaries in MRI scans. The Canny edge detection algorithm is employed as shown mathematically in Eq.(5).

$$E(x, y) = \nabla I(x, y) = \sqrt{\left(\frac{\partial I}{\partial x}\right)^2 + \left(\frac{\partial I}{\partial y}\right)^2} \quad (5)$$

where  $E(x, y)$  represents the edge intensity at coordinates  $(x, y)$ , and  $\frac{\partial I}{\partial x}, \frac{\partial I}{\partial y}$  are the image gradients along the  $x$  and  $y$  directions. The edges extracted using this method help in accurately delineating tumor regions, reflecting the precise prey detection capabilities of sea lions.

The optimized behavior of sea lions in focusing on specific prey areas inspires adaptive cropping of MRI images to focus on regions containing tumors. Adaptive cropping is defined mathematically as Eq.(6).

$$I_c(x, y) = \begin{cases} I(x, y), & \text{if } (x, y) \in R_t \\ 0 & \text{otherwise} \end{cases} \quad (6)$$

where,  $I_c(x, y)$  denotes the cropped image intensity,  $I(x, y)$  is the original intensity, and  $R_t$  represents the tumor region. This operation eliminates irrelevant areas, ensuring computational resources are concentrated on essential regions, akin to the sea lion's optimized targeting.

Sea lions effectively interpret information at multiple sensory levels. Multi-scale transformations replicate this behavior by creating image pyramids, ensuring hierarchical feature extraction as expressed mathematically in Eq.(7).

$$I_s(x, y, k) = I(x, y) * G(x, y, k) \quad (7)$$

Where,  $I_s(x, y, k)$  represents the scaled image at level  $k$ ,  $G(x, y, k)$  is the Gaussian kernel for scale  $k$ , and  $I(x, y)$  is the original image. Multi-scale analysis ensures that features of different sizes are captured, optimizing classification outcomes. The efficient preprocessing step in SLIA-RN50 systematically enhances MRI image quality by incorporating optimized strategies inspired by sea lions.

### 3.2. Region-Specific Focus

This phase is directly inspired by the sea lion's optimized ability to concentrate on specific prey regions amidst complex environments. This phase intends to direct computational resources toward areas of interest within MRI images, such as suspected tumor regions, while disregarding irrelevant portions. This ensures the model efficiently extracts meaningful features, thereby improving classification accuracy.

To emulate the sea lion's capacity to detect relevant regions in its environment, an adaptive attention mechanism is employed. This mechanism assigns higher weights to regions likely to contain tumors. Mathematically, attention weighting is defined as Eq.(8).

$$A(x, y) = \frac{\exp(S(x, y))}{\sum_{i, j} \exp(S(i, j))} \quad (8)$$

where,  $A(x, y)$  represents the attention weight at pixel location  $(x, y)$ , and  $S(x, y)$  denotes the saliency score derived from preliminary feature extraction. The normalization ensures that weights are distributed proportionally across the image, highlighting regions of interest while maintaining overall consistency. This reflects the optimized precision of sea lions in prioritizing key targets.

The saliency map is generated to emphasize tumor regions, simulating the sea lion's optimized focus on high-contrast stimuli. The saliency map is calculated using gradient-based backpropagation.

$$M_s(x, y) = \left| \frac{\partial L}{\partial I(x, y)} \right| \quad (9)$$

In Eq.(9), where  $M_s(x, y)$  denotes the saliency value at pixel location  $(x, y)$ ,  $L$  is the loss function, and  $I(x, y)$  represents the image intensity at  $(x, y)$ . The absolute gradient captures the sensitivity of the loss function to changes in pixel intensity, effectively highlighting tumor boundaries. This method aligns with the sea lion's optimized strategy of detecting subtle movements in prey.

To ensure computational resources are concentrated on relevant areas, a focused feature mask is applied. This mask isolates specific regions, excluding irrelevant portions of the image. The mask is defined as expressed in Eq.(10).

$$M_f(x, y) = \begin{cases} 1, & \text{if } (x, y) \in R_t \\ 0, & \text{otherwise} \end{cases} \quad (10)$$

where,  $M_f(x, y)$  represents the feature mask, and  $R_t$  denotes the tumor region identified using the saliency map. The multiplication of this mask with the original image ensures that only the tumor regions contribute to subsequent processing, reflecting the sea lion's optimized approach of targeting specific areas.

The optimized behavior of sea lions in adjusting their movements based on prey dynamics inspires dynamic window selection in region-specific focus. This step divides the image into overlapping windows and selects those containing high attention scores. The process is represented as Eq.(11).

$$W_d = \arg \max_{W_k} \sum_{(x,y) \in W_k} A(x, y) \quad (11)$$

where,  $W_d$  denotes the dynamically selected window,  $W_k$  represents a candidate window, and  $A(x, y)$  is the attention weight within  $W_k$ . By focusing on high-priority windows, this approach ensures optimal spatial allocation of computational resources, akin to the energy-efficient hunting strategies of sea lions.

After isolating key regions, the extracted features are integrated using weighted aggregation. This process consolidates information from various regions into a cohesive representation. The integration is expressed as Eq.(12)

$$F_{agg} = \sum_{k=1}^N w_k F_k \quad (12)$$

where  $F_{agg}$  represents the aggregated feature map,  $F_k$  denotes the feature map from region  $k$ ,  $w_k$  is the weight assigned to region  $k$ , and  $N$  is the total number of regions. This weighted aggregation enhances feature significance, mirroring the sea lion's ability to combine sensory inputs for optimized decision-making.

Sea lions adapt their focus dynamically, processing stimuli at multiple levels. This behavior is replicated through multi-layer region attention, which applies attention mechanisms at different network depths. The attention score at layer  $l$  is calculated as shown in Eq.(13).

$$A_l(x, y) = \frac{\sum_{i=1}^{N_l} S_l(i) \cdot W_l(i)}{N_l} \quad (13)$$

where,  $A_l(x, y)$  is the attention score at layer  $l$ ,  $S_l(i)$  represents the saliency score of feature  $i$  in layer  $l$ ,  $W_l(i)$  denotes the weight of feature  $i$ , and  $N_l$  is the total number of features in layer  $l$ . This multi-layer approach ensures that hierarchical features contribute to region-specific optimization.

To emulate the sea lion's energy-efficient strategies, region refinement is applied to minimize redundant computations. Regions are iteratively refined using confidence scores from a region proposal network (RPN).

$$C_r = \frac{\sum_{(x,y) \in R_p} P(x, y)}{|R_p|} \quad (14)$$

In Eq.(14), where  $C_r$  is the confidence score for the region  $R_p$ ,  $P(x, y)$  denotes the probability of pixel  $(x, y)$  belonging to the tumor region, and  $|R_p|$  is the total number of pixels in  $R_p$ . Regions with low confidence scores are excluded from further processing, ensuring optimized resource utilization. This approach enhances the model's ability to detect and classify tumors in MRI images with superior accuracy and efficiency.

### 3.3. Adaptive Learning Rate

The adaptive learning rate in SLIA-RN50 mirrors the sea lion's optimized ability to adjust movements and energy consumption in response to environmental changes. In the context of MRI classification, this step ensures efficient model training by dynamically modulating the learning rate, thereby enhancing convergence speed and reducing computational overhead. Inspired by the sea lion's adaptive behavior, the learning rate strategy in SLIA-RN50 prevents overshooting and underfitting while optimizing resource usage.

The learning rate is dynamically adjusted based on the gradient magnitude during training. This method reflects the sea lion's ability to fine-tune its actions when approaching prey. The adjustment is formulated as expressed Eq.(15).

$$\eta_t = \eta_0 \cdot \frac{1}{1 + \lambda \cdot t} \quad (15)$$

where,  $\eta_t$  represents the learning rate at time step  $t$ ,  $\eta_0$  is the initial learning rate,  $\lambda$  is the decay rate, and  $t$  denotes the current iteration. The decay rate  $\lambda$  ensures a gradual reduction of the learning rate, allowing the model to focus on fine-tuning weights during later training stages, similar to the sea lion's

optimized effort conservation during precision movements.

To maintain stability in weight updates, the learning rate is scaled based on the gradient norm. The scaling factor is calculated as shown in Eq.(16).

$$\eta_s = \frac{\eta}{1 + \|g\|} \quad (16)$$

Where  $\eta_s$  denotes the scaled learning rate,  $\eta$  is the base learning rate, and  $\|g\|$  represents the norm of the gradient vector. This adjustment ensures stability during large weight updates, aligning with the sea lion's optimized balance between agility and precision when navigating turbulent waters.

Momentum is adaptively integrated into the learning rate to enhance convergence, inspired by the sea lion's ability to capitalize on accumulated energy during swift directional changes. The momentum-augmented learning rate is expressed mathematically in Eq.(17) and Eq.(18).

$$v_t = \beta \cdot v_{t-1} + (1 - \beta) \cdot g_t \quad (17)$$

$$\eta_t = \eta \cdot v_t \quad (18)$$

Where  $v_t$  is the velocity term at time step  $t$ ,  $\beta$  is the momentum coefficient,  $g_t$  is the gradient at time  $t$ , and  $\eta_t$  is the updated learning rate. The momentum component amplifies learning rate adjustments based on past gradients, ensuring smooth and efficient convergence, akin to the sea lion's use of inertia in optimized swimming patterns.

Inspired by the sea lion's gradual decrease in effort as it nears prey, time-based decay ensures that the learning rate decreases consistently over iterations. This decay strategy is expressed as Eq.(19).

$$\eta_t = \eta_0 \cdot e^{-\alpha \cdot t} \quad (19)$$

where  $\eta_t$  is the learning rate at iteration  $t$ ,  $\eta_0$  is the initial learning rate, and  $\alpha$  is the decay constant. The exponential decay ensures that learning rate adjustments become smaller as training progresses, promoting precise weight updates during later stages.

The optimized behavior of sea lions to avoid excessive energy expenditure is reflected in learning rate clipping, which constrains updates within a specific range. The clipped learning rate is defined mathematically in Eq.(20).

$$\eta_c = \min(\eta_{max}, \max(\eta_{min}, \eta_t)) \quad (20)$$

where,  $\eta_c$  is the clipped learning rate,  $\eta_{max}$  and  $\eta_{min}$  are the maximum and minimum allowable rates, respectively, and  $\eta_t$  is the unadjusted learning rate. This technique ensures controlled updates, preventing extreme fluctuations in weight changes and maintaining optimization efficiency.

The cyclical behavior of sea lions, characterized by alternating between swift and slow movements, inspires cosine annealing for learning rate modulation. The learning rate at iteration  $t$  is computed as shown in Eq.(21).

$$\eta_t = \eta_{min} + \frac{\eta_{max} - \eta_{min}}{2} \left( 1 + \cos\left(\frac{t\pi}{T}\right) \right) \quad (21)$$

where  $\eta_t$  is the annealed learning rate,  $\eta_{min}$  and  $\eta_{max}$  are the minimum and maximum learning rates,  $T$  represents the total number of iterations, and  $t$  is the current iteration. Cosine annealing introduces periodicity in the learning rate, mimicking the sea lion's energy-efficient behavioral cycles.

Inspired by the sea lion's ability to allocate focus to specific sensory inputs, layer-specific learning rates are introduced to optimize updates for different network layers. The learning rate for layer  $l$  is calculated as expressed mathematically in Eq.(22).

$$\eta_l = \eta \cdot \frac{1}{\sqrt{1 + d_l}} \quad (22)$$

where  $\eta_l$  represents the learning rate for layer  $l$ ,  $\eta$  is the base learning rate, and  $d_l$  denotes the depth of layer  $l$ . This adjustment ensures that deeper layers, which require more fine-tuning, receive smaller learning rate updates, aligning with the sea lion's optimized focus on critical sensory information. Adaptive learning rate strategies ensure that the model dynamically adjusts to the complexity of MRI data during training.

### 3.4. Energy-Efficient Architecture

This phase draws direct inspiration from the sea lion's optimized ability to conserve energy during long-distance swimming and bursts of activity. By adapting computational resources to the requirements of the task, this architecture ensures minimal energy usage while maintaining optimal performance in MRI classification. The design leverages modularity, adaptive computations, and resource-aware operations to align with the resourceful behaviors of the sea lion.

Inspired by the sea lion's segmented body movements, the architecture incorporates modular layer design to distribute computational load efficiently. The modularity is expressed mathematically as Eq.(23).

$$f(x) = \sum_{i=1}^N \sigma(W_i \cdot x + b_i) \quad (23)$$

where,  $f(x)$  represents the output of the modular layers,  $N$  is the total number of modules,  $W_i$  denotes the weights for module  $i$ ,  $x$  is the input,  $b_i$  is the bias term, and  $\sigma$  is the activation function. Each module processes a specific aspect of the input, ensuring that computations are performed in smaller, energy-efficient units, akin to the segmented effort optimization seen in sea lions.

Depth-wise separable convolutions are incorporated to reduce the number of parameters while retaining feature extraction capabilities. This process is mathematically formulated as Eq.(24).

$$Y(x, y) = \sum_{c=1}^C K_c(x, y) * I_c(x, y) \quad (24)$$

where,  $Y(x, y)$  represents the output feature map at the position  $(x, y)$ ,  $K_c(x, y)$  is the depth-wise convolution kernel for channel  $c$ ,  $I_c(x, y)$  is the input feature map, and  $C$  denotes the number of channels. Depth-wise convolutions operate separately on each channel, minimizing computational overhead, and reflecting the sea lion's ability to streamline movements for energy conservation.

The architecture includes energy-aware skip connections, inspired by the sea lion's optimized redirection of energy when encountering obstacles. These skip connections ensure efficient gradient flow and avoid redundant computations. Mathematically, this is represented in Eq.(25).

$$h(x) = F(x, \{W_i\}) + x \quad (25)$$

where,  $h(x)$  is the output of the skip connection,  $F(x, \{W_i\})$  represents the learned residual mapping,  $x$  is the input, and  $\{W_i\}$  denotes the weights of the residual layers. The addition operation enables the network to reuse previously computed features, thereby reducing energy consumption while maintaining model accuracy.

Grouped convolutions divide input channels into groups, processing them independently to reduce computational complexity. This operation is mathematically expressed as Eq.(26).

$$Y_g(x, y) = \sum_{k=1}^G K_g(k, x, y) * I_g(k, x, y) \quad (26)$$

Where  $Y_g(x, y)$  represents the output of grouped convolutions at the position  $(x, y)$ ,  $K_g(k, x, y)$  is the convolution kernel for group  $k$ ,  $I_g(k, x, y)$  is the input for group  $k$ , and  $G$  is the total number of groups. Grouped convolutions optimize resource allocation, mimicking the sea lion's energy-efficient distribution of muscle effort during swimming.

Regularization techniques inspired by the sea lion's lean and agile physique are applied to enforce sparsity in weight matrices. This reduces unnecessary computations without compromising performance. Sparsity regularization is expressed as Eq.(27).

$$R_s = \lambda \sum_{i=1}^N |W_i| \quad (27)$$

where,  $R_s$  represents the sparsity regularization term,  $\lambda$  is the regularization coefficient,  $N$  is the total number of parameters, and  $W_i$  denotes individual weights. By penalizing large weight magnitudes, sparsity regularization reduces parameter redundancy, enhancing energy efficiency.

Adaptive batch processing ensures that computational resources are allocated dynamically based on input complexity, inspired by the sea lion's adaptive hunting strategies. The batch size is determined as Eq.(28).

$$B_t = \left\lfloor \frac{C_{max} - C_t}{C_{avg}} \right\rfloor \quad (28)$$

where  $B_t$  represents the batch size at time  $t$ ,  $C_{max}$  denotes the maximum computational capacity,  $C_t$  is the current computational load, and  $C_{avg}$  is the average complexity of the input data. This adaptive mechanism ensures optimal resource usage, aligning with the sea lion's efficient energy allocation strategies.

Inspired by the sea lion's ability to process information from multiple sensory inputs, multi-scale feature fusion integrates features at different resolutions. This is represented mathematically in Eq.(29).

$$F_m = \sum_{s=1}^S w_s \cdot F_s \quad (29)$$

where  $F_m$  denotes the fused feature map,  $F_s$  represents the feature map at scale  $s$ ,  $w_s$  is the weight assigned to scale  $s$ , and  $S$  is the total number of scales. Multi-scale fusion captures hierarchical features

efficiently, enhancing classification performance while maintaining energy efficiency.

### 3.5. Hierarchical Feature Extraction

Hierarchical feature extraction in SLIA-RN50 is inspired by the sea lion's ability to analyze multiple sensory inputs simultaneously, focusing on hierarchical layers of information to identify prey and respond effectively. This step in the architecture involves extracting features at different levels of abstraction, enabling efficient and accurate MRI classification. The hierarchical structure ensures that the model captures fine-grained details and broader contextual patterns while minimizing redundancy.

The multi-layered structure of SLIA-RN50 extracts features progressively, mirroring the sea lion's sequential analysis of sensory inputs. The feature learning process is mathematically expressed as Eq.(30).

$$F^l(x, y) = \sigma(W^l * F^{l-1}(x, y) + b^l) \quad (30)$$

where  $F^l(x, y)$  represents the feature map at layer  $l$ ,  $W^l$  denotes the weight matrix for layer  $l$ ,  $F^{l-1}(x, y)$  is the input feature map from the previous layer,  $b^l$  is the bias term, and  $\sigma$  is the activation function. This hierarchical process ensures that each layer extracts increasingly abstract features, reflecting the sea lion's optimized ability to integrate details over time.

Inspired by the sea lion's capacity to perceive details at varying depths and distances, pyramid feature extraction captures information at multiple scales. The pyramid feature extraction process is defined as Eq.(31).

$$F_p(x, y, s) = G_s * F(x, y) \quad (31)$$

where,  $F_p(x, y, s)$  represents the scaled feature map for scale  $s$ ,  $G_s$  is the Gaussian kernel at scale  $s$ , and  $F(x, y)$  denotes the original feature map. Pyramid extraction ensures that features of varying spatial resolutions are captured, enabling the identification of tumors of different sizes and shapes, and optimizing classification accuracy.

Spatial refinement optimizes feature localization, akin to the sea lion's ability to pinpoint prey with precision. Refinement is achieved by applying spatial attention weights as represented mathematically in Eq.(32).

$$F_r(x, y) = A_s(x, y) \cdot F(x, y) \quad (32)$$

where,  $F_r(x, y)$  denotes the refined feature map,  $A_s(x, y)$  represents the spatial attention weight, and  $F(x, y)$  is the input feature map. Spatial attention emphasizes regions containing critical information while suppressing irrelevant areas, reflecting the optimized sensory focus of sea lions.

Channel-wise aggregation consolidates features across channels, mirroring the sea lion's integration of multi-sensory inputs. The aggregation process is formulated as Eq.(33).

$$F_c(x, y) = \sum_{k=1}^C w_k \cdot F_k(x, y) \quad (33)$$

where  $F_c(x, y)$  represents the aggregated feature map,  $F_k(x, y)$  is the feature map for channel  $k$ ,  $w_k$  is the weight assigned to channel  $k$ , and  $C$  denotes the total number of channels. This method reduces dimensionality while preserving critical information, optimizing computational efficiency and feature richness.

The integration of temporal features ensures the extraction of sequential patterns, analogous to the sea lion's ability to process temporal variations in prey movements. Temporal integration is defined as Eq.(34).

$$F_t(x, y) = \alpha \cdot F_t^{prev}(x, y) + (1 - \alpha) \cdot F(x, y) \quad (34)$$

where  $F_t(x, y)$  represents the temporally integrated feature map,  $F_t^{prev}(x, y)$  is the feature map from the previous time step,  $F(x, y)$  is the current feature map, and  $\alpha$  is the integration coefficient. This approach captures dynamic changes in MRI images, enhancing the model's ability to detect evolving patterns, such as tumor growth.

Residual feature fusion combines features across layers, ensuring that hierarchical information is retained without redundancy. The fusion process is mathematically expressed as Eq.(35).

$$F_f(x, y) = \sum_{l=1}^L \alpha_l \cdot F^l(x, y) \quad (35)$$

Where  $F_f(x, y)$  represents the fused feature map,  $F^l(x, y)$  denotes the feature map at layer  $l$ ,  $\alpha_l$  is the weight assigned to layer  $l$ , and  $L$  is the total number of layers. By consolidating hierarchical features, this method ensures a comprehensive representation of the input data, reflecting the optimized integration of sensory inputs by sea lions.

Gradient-weighted prioritization emphasizes features contributing most to the classification decision, inspired by the sea lion's

optimized focus on critical sensory inputs. The prioritization process is expressed as Eq.(36).

$$F_g(x, y) = \nabla_w \cdot F(x, y) \quad (36)$$

where  $F_g(x, y)$  represents the gradient-weighted feature map,  $\nabla_w$  denotes the gradient concerning the weights, and  $F(x, y)$  is the input feature map. This technique ensures that the most relevant features are prioritized, reducing computational overhead and enhancing classification accuracy. Hierarchical feature extraction leverages these optimized methods to capture detailed and contextual information from MRI images. Each aspect of this process is inspired by the sea lion's natural ability to integrate information hierarchically, ensuring an efficient and accurate analysis framework tailored for MRI classification tasks.

### 3.6. Dynamic Pooling Strategies

Dynamic pooling strategies in SLIA-RN50 are inspired by the sea lion's optimized ability to adaptively adjust its focus and energy based on environmental demands. These strategies ensure that the architecture captures critical features from MRI images by dynamically adapting the pooling operation to the complexity and scale of the input. This approach enhances both the spatial representation and computational efficiency, reflecting the sea lion's precise and adaptive behavior in various aquatic conditions.

Adaptive average pooling ensures that feature maps are resized to a fixed dimension, maintaining spatial flexibility. This operation is expressed mathematically in Eq.(37).

$$P_{avg}(x, y) = \frac{1}{|R_{x,y}|} \sum_{(i,j) \in R_{x,y}} F(i, j) \quad (37)$$

where  $P_{avg}(x, y)$  represents the pooled value at the position  $(x, y)$ ,  $R_{x,y}$  denotes the receptive field corresponding to  $(x, y)$ , and  $F(i, j)$  is the feature value within the receptive field. Adaptive average pooling balances feature extraction across varying input sizes, reflecting the sea lion's ability to maintain focus regardless of environmental variability.

Max-entropy pooling is employed to prioritize regions containing the highest amount of information, akin to the sea lion's focus on high-value targets in its surroundings. The operation is expressed mathematically in Eq.(38).

$$P_{ent}(x, y) = \max_{(i,j) \in R_{x,y}} H(F(i, j)) \quad (38)$$

where,  $P_{ent}(x, y)$  represents the pooled entropy value,  $H(F(i, j))$  is the entropy of the feature value  $F(i, j)$ , and  $R_{x,y}$  is the receptive field for the position  $(x, y)$ . This strategy ensures that high-entropy regions, indicative of critical information, are preserved, optimizing the pooling process.

Spatially weighted pooling emphasizes regions with higher attention weights, mirroring the sea lion's optimized focus on specific sensory stimuli. The pooling operation is expressed as Eq.(39).

$$P_w(x, y) = \sum_{(i,j) \in R_{x,y}} W(i, j) \cdot F(i, j) \quad (39)$$

where,  $P_w(x, y)$  represents the weighted pooled value,  $W(i, j)$  denotes the spatial attention weight,  $F(i, j)$  is the feature value, and  $R_{x,y}$  is the receptive field. By focusing on weighted regions, this pooling strategy preserves critical spatial details while suppressing irrelevant information.

Pyramid pooling captures multi-scale feature representations, reflecting the sea lion's ability to integrate sensory inputs at varying levels of detail. The operation involves pooling over multiple scales.

$$P_p^s = \frac{1}{|R^s|} \sum_{(i,j) \in R^s} F(i, j) \quad (40)$$

In Eq.(40), where  $P_p^s$  represents the pooled value at scale  $s$ ,  $R^s$  denotes the receptive field at scale  $s$ , and  $F(i, j)$  is the feature value. Multi-scale pooling ensures that features from both coarse and fine-grained regions are effectively captured, optimizing the classification of tumors with diverse sizes and structures.

Stochastic pooling introduces variability by selecting pooled values probabilistically, inspired by the sea lion's dynamic behavior in adapting to unpredictable conditions. The probability of selecting a feature value is defined as Eq.(41).

$$P_{st}(F(i, j)) = \frac{F(i, j)}{\sum_{(k,l) \in R_{x,y}} F(k, l)} \quad (41)$$

The pooled value is then sampled according to this probability distribution. Stochastic pooling captures diverse patterns, enhancing robustness to variations in MRI data.

Energy-efficient pooling reduces the computational complexity of pooling operations, aligning with the sea lion's optimized energy usage during foraging.

$$P_e(x, y) = \frac{\sum_{(i,j) \in R_{x,y}} F(i, j) \cdot \exp(-\|F(i, j) - \mu\|^2 / 2\sigma^2)}{\sum_{(i,j) \in R_{x,y}} \exp(-\|F(i, j) - \mu\|^2 / 2\sigma^2)} \quad (42)$$

In Eq.(42), where  $P_e(x, y)$  represents the energy-efficient pooled value,  $\mu$  is the mean feature value, and  $\sigma$  is the standard deviation. This strategy ensures that pooling emphasizes informative regions while minimizing energy consumption, reflecting the sea lion's resourceful nature.

### 3.7. Precision Optimization

Precision optimization emulates the sea lion's ability to make highly accurate and targeted movements while conserving energy. This step involves refining the classification process by optimizing weight updates, improving feature representation, and reducing errors. Inspired by the sea lion's precise hunting strategies, the techniques used ensure that the model achieves high classification accuracy for MRI scans.

Gradient scaling adjusts the magnitude of weight updates to maintain precision during training. This is achieved through the formulation which is defined as Eq.(43).

$$\Delta W_t = \eta \cdot \frac{gt}{\sqrt{v_t + \epsilon}} \quad (43)$$

where  $\Delta W_t$  represents the weight update at time  $t$ ,  $\eta$  is the learning rate,  $gt$  is the gradient at time  $t$ ,  $v_t$  is the moving average of squared gradients, and  $\epsilon$  is a small constant for numerical stability. Gradient scaling prevents excessively large updates, enabling precise adjustments to weights, which reflects the optimized accuracy of sea lions in targeting prey.

Loss function regularization ensures that errors are minimized while maintaining stability during optimization. This is achieved by combining a primary loss function with a regularization term which is represented mathematically in Eq.(44).

$$L_{reg} = L_{primary} + \lambda \cdot \|W\|^2 \quad (44)$$

where,  $L_{reg}$  is the regularized loss,  $L_{primary}$  represents the primary loss function (e.g., cross-entropy),  $\lambda$  is the regularization coefficient, and  $\|W\|^2$  denotes the squared norm of weights. Regularization discourages overly complex models, ensuring that the network generalizes well to unseen data while maintaining precision.

Inspired by the sea lion's ability to prioritize high-certainty actions, confidence-weighted prediction refinement emphasizes outputs with

higher predictive confidence. This refinement is mathematically expressed as Eq.(45).

$$P_{ref}(c) = \frac{P(c)}{\sum_{i=1}^C P(i)} \quad (45)$$

where,  $P_{ref}(c)$  represents the refined probability of class  $c$ ,  $P(c)$  denotes the initial probability of class  $c$ , and  $C$  is the total number of classes. Refining predictions based on confidence levels enhances the reliability of classification decisions, optimizing precision.

Feature normalization ensures that input features are standardized for stable and precise representation. This step is expressed mathematically in Eq.(46).

$$F_{norm}(x) = \frac{F(x) - \mu}{\sigma} \quad (46)$$

where,  $F_{norm}(x)$  represents the normalized feature,  $F(x)$  is the original feature value,  $\mu$  is the mean of the feature values, and  $\sigma$  is the standard deviation. Normalization reduces variability in feature scales, ensuring that the network focuses on the most relevant patterns in MRI data.

Class-specific loss weighting assigns different weights to classes based on their prevalence and importance, mirroring the sea lion's strategy of focusing on the most critical targets. The weighted loss function is defined as Eq.(47).

$$L_{weighted} = \sum_{c=1}^C w_c \cdot L_c \quad (47)$$

where,  $L_{weighted}$  represents the weighted loss,  $w_c$  is the weight assigned to class  $c$ ,  $L_c$  denotes the loss for class  $c$ , and  $C$  is the total number of classes. By prioritizing underrepresented or critical classes, this approach enhances the precision of classification across different tumor types.

Adaptive thresholding dynamically adjusts decision thresholds based on the distribution of output probabilities, reflecting the sea lion's optimized decision-making under varying conditions. The threshold adjustment is expressed as Eq.(48).

$$T_{adaptive} = \mu_p + \alpha \cdot \sigma_p \quad (48)$$

where,  $T_{adaptive}$  is the adaptive threshold,  $\mu_p$  is the mean probability of the outputs,  $\sigma_p$  is the standard deviation of probabilities, and  $\alpha$  is a scaling factor. This approach ensures that decisions are fine-tuned to maximize precision while reducing false positives and negatives.

### 3.8. Multi-Scale Feature Integration

Multi-scale feature integration draws inspiration from the sea lion’s ability to process visual and sensory inputs at varying distances and depths. This approach ensures that features from multiple scales are captured and combined to enhance the model’s ability to identify patterns and abnormalities in MRI scans. Multi-scale integration optimizes the classification process by encompassing both fine-grained details and broader contextual information.

Multi-scale feature extraction begins by generating feature maps at different resolutions, akin to the sea lion’s dynamic sensory adjustment. The process is expressed mathematically as Eq.(49).

$$F_s(x, y) = F(x, y) * G_s(x, y) \quad (49)$$

where,  $F_s(x, y)$  represents the feature map at scale  $s$ ,  $F(x, y)$  denotes the input feature map, and  $G_s(x, y)$  is the Gaussian kernel at scale  $s$ . By applying Gaussian filters, the architecture captures features of varying spatial granularity, ensuring a comprehensive representation of the input.

To ensure consistency across scales, spatial alignment is employed to map feature maps from different resolutions onto a common spatial domain. The alignment operation is mathematically expressed in Eq.(50).

$$F_a(x, y) = \sum_{(i,j) \in R_{x,y}} F_s(i, j) \cdot w_{align}(i, j) \quad (50)$$

where,  $F_a(x, y)$  represents the spatially aligned feature,  $F_s(i, j)$  denotes the feature map at scale  $s$ ,  $w_{align}(i, j)$  is the alignment weight, and  $R_{x,y}$  is the receptive field for position  $(x, y)$ . Spatial alignment preserves critical spatial relationships, enabling seamless integration of multi-scale features.

Inspired by the sea lion’s optimized focus on the most relevant sensory inputs, weighted aggregation is applied to prioritize features from specific scales. The aggregation process is represented mathematically in Eq.(51).

$$F_{agg}(x, y) = \sum_{s=1}^S w_s \cdot F_s(x, y) \quad (51)$$

where,  $F_{agg}(x, y)$  represents the aggregated feature map,  $w_s$  is the weight assigned to scale  $s$ ,  $F_s(x, y)$  denotes the feature map at scale  $s$ , and  $S$  is the total number of scales. By assigning weights based on scale relevance, this step optimizes the

integration process, reflecting the sea lion’s strategic prioritization.

Hierarchical fusion combines features from multiple network layers to capture hierarchical information. This fusion is expressed mathematically in Eq.(52).

$$F_h(x, y) = \sum_{l=1}^L \alpha_l \cdot F_l(x, y) \quad (52)$$

where,  $F_h(x, y)$  denotes the hierarchically fused feature map,  $F_l(x, y)$  is the feature map at layer  $l$ ,  $\alpha_l$  represents the weight assigned to layer  $l$ , and  $L$  is the total number of layers. Hierarchical fusion ensures that both low-level and high-level features contribute to the final representation, aligning with the sea lion’s ability to integrate layered sensory inputs.

Channel attention is employed to refine the integrated features by emphasizing critical channels. The attention mechanism is represented mathematically in Eq.(53).

$$F_{ref}(x, y, c) = F_{agg}(x, y, c) \cdot A(c) \quad (53)$$

where,  $F_{ref}(x, y, c)$  represents the refined feature map for channel  $c$ ,  $F_{agg}(x, y, c)$  is the aggregated feature map for channel  $c$ , and  $A(c)$  denotes the attention weight for channel  $c$ . This mechanism enhances the focus on important channels, optimizing the overall representation for classification.

Temporal scaling is introduced to capture dynamic patterns over time, inspired by the sea lion’s ability to adjust focus based on changing stimuli. Temporal scaling is expressed mathematically in Eq.(54).

$$F_t(x, y) = \sum_{t=1}^T \beta_t \cdot F_{agg}(x, y, t) \quad (54)$$

where,  $F_t(x, y)$  represents the temporally scaled feature map,  $F_{agg}(x, y, t)$  denotes the aggregated feature map at time  $t$ ,  $\beta_t$  is the weight for time step  $t$ , and  $T$  is the total number of time steps. Temporal scaling ensures that evolving patterns in MRI data are captured effectively.

To optimize the classification process, scale-specific loss weighting assigns different weights to losses computed at various scales. The loss function is expressed mathematically in Eq.(55).

$$L_{scale} = \sum_{s=1}^S w_s \cdot L_s \quad (55)$$

where,  $L_{scale}$  represents the scale-specific loss,  $w_s$  is the weight assigned to scale  $s$ ,  $L_s$  denotes the loss computed at scale  $s$ , and  $S$  is the total number of scales. This approach balances contributions from different scales, enhancing the precision and robustness of the classification process.

### 3.9. Collaborative Filtering Layers

Collaborative filtering layers in SLIA-RN50 emulate the cooperative behavior observed in sea lions, where individuals in groups work together to enhance hunting efficiency. This step integrates multiple layers to refine features collaboratively, improving the model's capacity to identify subtle and critical patterns in MRI images. The strategy ensures the fusion of features across layers, reducing redundancy and enhancing classification precision.

Cross-layer correlation aligns feature maps across layers to ensure consistency in feature representation. The correlation is mathematically expressed as Eq.(56).

$$C_{i,j}(x,y) = \frac{\sum_{(x,y)} F_i(x,y) \cdot F_j(x,y)}{\sqrt{\sum_{(x,y)} F_i^2(x,y) \cdot \sum_{(x,y)} F_j^2(x,y)}} \quad (56)$$

where,  $C_{i,j}(x,y)$  represents the correlation between layers  $i$  and  $j$  at position  $(x,y)$ , and  $F_i(x,y)$ ,  $F_j(x,y)$  denote the feature maps of layers  $i$  and  $j$ . By aligning features through cross-layer correlation, the architecture optimizes consistency in representation, reflecting the sea lion's synchronized movements during group hunting.

Weighted feature blending combines feature maps from different layers to collaboratively enhance representation. This blending is defined as shown in Eq.(57).

$$F_b(x,y) = \sum_{l=1}^L w_l \cdot F_l(x,y) \quad (57)$$

where,  $F_b(x,y)$  denotes the blended feature map,  $w_l$  is the weight assigned to layer  $l$ ,  $F_l(x,y)$  represents the feature map at layer  $l$ , and  $L$  is the total number of layers. Weighted blending ensures that contributions from relevant layers are prioritized, mirroring the optimized focus of sea lions on the most promising prey in collaborative scenarios.

Attention-based recalibration adjusts feature importance by applying attention weights derived from a global context. This recalibration is expressed mathematically in Eq.(58).

$$F_r(x,y) = F_b(x,y) \cdot A(x,y) \quad (58)$$

where,  $F_r(x,y)$  represents the recalibrated feature map,  $F_b(x,y)$  denotes the blended feature map, and  $A(x,y)$  is the attention weight at position  $(x,y)$ . Attention-based recalibration enhances critical regions while suppressing less relevant areas, reflecting the optimized sensory focus of sea lions.

Iterative filtering refines features progressively across layers, inspired by the sea lion's continuous adjustments during cooperative activities. The iterative process is mathematically defined as Eq.(59).

$$F_t(x,y) = F_{t-1}(x,y) + \alpha \cdot \nabla F_{t-1}(x,y) \quad (59)$$

where,  $F_t(x,y)$  denotes the feature map at iteration  $t$ ,  $F_{t-1}(x,y)$  represents the feature map from the previous iteration,  $\nabla F_{t-1}(x,y)$  is the gradient of the feature map, and  $\alpha$  is the step size. Iterative filtering ensures that features are refined incrementally, enhancing precision in representation.

Collaborative error minimization reduces discrepancies between feature maps by enforcing consistency through optimization. The minimization process is expressed as Eq.(60).

$$E_{collab} = \sum_{i,j=1}^L \|F_i(x,y) - F_j(x,y)\|^2 \quad (60)$$

where,  $E_{collab}$  represents the collaborative error,  $F_i(x,y) - F_j(x,y)$  denote the feature maps of layers  $i$  and  $j$ , and  $L$  is the total number of layers. By minimizing errors collaboratively, the architecture ensures harmonized feature representation, optimizing its classification capacity.

Global feature fusion integrates all layers to create a holistic representation of the input data, analogous to the sea lion's ability to combine sensory inputs for optimal decision-making. The fusion process is defined as shown in Eq.(61).

$$F_g(x,y) = \sum_{l=1}^L \beta_l \cdot F_l(x,y) \quad (61)$$

where,  $F_g(x,y)$  denotes the globally fused feature map,  $F_l(x,y)$  represents the feature map of layer  $l$ ,  $\beta_l$  is the fusion weight for layer  $l$ , and  $L$  is the total number of layers. Global fusion captures comprehensive information, enhancing the robustness and precision of MRI classification.

### 3.10. Real-Time Adaptability

Real-time adaptability in SLIA-RN50 replicates the sea lion's optimized ability to respond dynamically to changing environments during navigation and hunting. This step enables the architecture to adapt to incoming MRI data by dynamically fine-tuning its processing pipelines based on the complexity and context of the input. Real-time adaptability ensures that the model remains efficient and accurate, even when faced with variations in image quality, patient-specific characteristics, or unexpected abnormalities.

Adaptive data augmentation dynamically modifies input data during runtime to address variations in MRI scans, such as differences in resolution or contrast. The augmentation process is expressed as Eq.(62).

$$I_{aug}(x, y) = I(x, y) \cdot \gamma + \beta \quad (62)$$

where,  $I_{aug}(x, y)$  represents the augmented image,  $I(x, y)$  is the original image,  $\gamma$  is the scaling factor for intensity adjustment, and  $\beta$  is the bias term for contrast enhancement. Adaptive augmentation mimics the sea lion's ability to adjust its sensory perception in real time to optimize data input for further processing.

Runtime feature selection identifies and processes the most relevant features dynamically based on the input context. The selection process is defined as Eq.(63).

$$F_{sel}(x, y) = \sum_{i=1}^N w_i \cdot F_i(x, y) \cdot \delta_i \quad (63)$$

where,  $F_{sel}(x, y)$  denotes the selected feature map,  $F_i(x, y)$  represents the feature map for layer  $i$ ,  $w_i$  is the weight for layer  $i$ ,  $\delta_i$  is a binary indicator determining whether layer  $i$  is selected, and  $N$  is the total number of layers. By activating only the most relevant features, this method reduces redundancy and optimizes computational efficiency, similar to the sea lion's selective energy usage in dynamic conditions.

Dynamic learning rate adjustment refines model parameters during runtime based on the evolving complexity of the task. This adjustment is mathematically represented as Eq.(64).

$$\eta_t = \eta_0 \cdot \frac{1}{1 + \lambda \cdot C_t} \quad (64)$$

where,  $\eta_t$  is the learning rate at time  $t$ ,  $\eta_0$  denotes the initial learning rate,  $\lambda$  is the decay coefficient, and  $C_t$  represents the complexity of the current input. Adjusting the learning rate dynamically ensures

optimal parameter updates, reflecting the sea lion's real-time adaptation to changing environmental stimuli.

Real-time loss adjustment modifies the loss function dynamically based on the complexity and variability of the input. The adjusted loss function is defined as Eq.(65).

$$L_{real}(t) = L_{primary}(t) + \alpha \cdot \frac{\partial L_{primary}(t)}{\partial I(t)} \quad (65)$$

where,  $L_{real}(t)$  represents the real-time adjusted loss,  $L_{primary}(t)$  denotes the primary loss at time  $t$ ,  $\alpha$  is the adjustment coefficient, and  $\frac{\partial L_{primary}(t)}{\partial I(t)}$  is the gradient of the primary loss concerning the input. This adjustment ensures that the model learns effectively from variable data while maintaining stability in its predictions.

Temporal data integration combines information from sequential MRI inputs to provide a comprehensive analysis of dynamic patterns. This integration operation is expressed mathematically as Eq.(66).

$$F_t(x, y) = \sum_{k=1}^T w_k \cdot F_k(x, y) \quad (66)$$

where,  $F_t(x, y)$  represents the temporally integrated feature map,  $F_k(x, y)$  denotes the feature map at time step  $k$ ,  $w_k$  is the weight assigned to time step  $k$ , and  $T$  is the total number of time steps. Temporal integration captures evolving abnormalities, enhancing the adaptability of the architecture to dynamic medical imaging scenarios.

Context-aware decision thresholding adjusts classification thresholds dynamically based on the distribution of predictions.

$$T_{context} = \mu_p + \sigma_p \cdot \phi(C_t) \quad (67)$$

In Eq.(67), where  $T_{context}$  denotes the context-aware threshold,  $\mu_p$  is the mean probability,  $\sigma_p$  is the standard deviation of probabilities, and  $\phi(C_t)$  is a scaling function based on the complexity  $C_t$ . By adapting thresholds to the input context, this method ensures precise and reliable classification decisions, mirroring the sea lion's ability to make real-time decisions during group coordination.

#### 4. ABOUT DATASET AND METRICS

The Brain Tumor MRI Dataset is an extensive collection of magnetic resonance imaging (MRI) scans, facilitating research in deep learning-based tumor classification. This dataset contains

7023 images, systematically divided into training and testing subsets. The training set comprises 5712 images, while the testing set includes 1311 images, ensuring reliable model evaluation. Each image is a T1-weighted grayscale MRI scan, stored in JPEG format, making it suitable for integration into machine learning frameworks. The dataset includes annotated tumor locations, assisting in segmentation and feature extraction tasks. Several features enhance its usability, including tumor size variations, morphological differences, and spatial distributions. The images support preprocessing techniques such as histogram equalization, noise reduction, and edge detection, improving classification accuracy. The dataset allows for image augmentation, including rotation, flipping, and contrast adjustments, ensuring robust deep learning model training. This dataset serves as a foundation for developing advanced deep learning models, particularly CNN-based architectures, for early tumor detection. The structured annotations contribute to enhancing computer-aided diagnosis (CAD) systems, enabling improved clinical decision-making in oncology and medical imaging research.

## 5. OUTCOMES AND DEBATES

Results and discussions provide a detailed evaluation of the model's performance based on key classification metrics. This section interprets the numerical results to highlight improvements and comparative efficiency in MRI classification. The focus remains on classification accuracy and F-measure to assess the predictive capability of the models. Classification accuracy represents the proportion of correctly classified instances among the total number of predictions. A higher classification accuracy indicates better overall performance in distinguishing between tumor and non-tumor regions. The results indicate that SLIA-ResNet50 achieves the highest classification accuracy at 74.8280, significantly outperforming PD-CNN (57.7830) and ABT-DCNN (60.8970). This improvement reflects the optimized hierarchical feature extraction and real-time adaptability integrated into SLIA-ResNet50. The increased classification accuracy signifies enhanced decision-making capabilities, reducing false predictions and improving reliability in medical imaging.

F-measure balances precision and recall, making it a crucial metric for evaluating model performance in unbalanced datasets. Higher values of F-measure suggest superior effectiveness in

identifying positive cases while minimizing false negatives and false positives. SLIA-ResNet50 achieves the highest F-measure of 76.2658, compared to 58.6274 for PD-CNN and 62.1634 for ABT-DCNN. This improvement validates the impact of multi-scale feature integration and collaborative filtering layers, which contribute to refined decision boundaries and reduced misclassification rates.

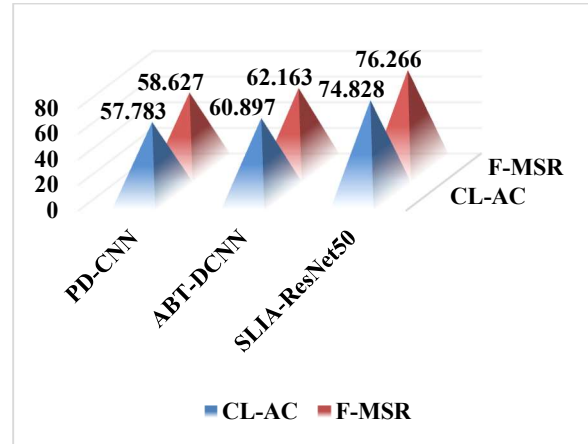


Fig 2. Classification Accuracy and F-Measure

Fig2, presents a comparative analysis of classification accuracy and F-measure, further illustrating the substantial advancements introduced by SLIA-ResNet50. The observed enhancements indicate that bio-inspired optimization significantly improves classification robustness, contributing to more reliable MRI-based tumor detection.

The “Fowlkes-Mallows Index” (FMI) measures the geometric mean of precision and recall, evaluating the balance between correctly classified positive instances and overall predictive performance. A higher FMI value indicates an improved ability to correctly identify true positives while minimizing false positives. The results show that SLIA-ResNet50 achieves an FMI of 76.374, significantly surpassing PD-CNN (58.868) and ABT-DCNN (62.391). The increase in FMI confirms the optimized adaptability of SLIA-ResNet50, which ensures precise classification by effectively distinguishing tumor regions in MRI scans.

The “Matthews Correlation Coefficient” (MCC) is a balanced metric for binary classification, considering true and false positives and negatives to provide a reliable measure of predictive accuracy. MCC values closer to 1 indicate strong correlation and better classification reliability. SLIA-ResNet50 achieves the highest MCC score of 49.950,

compared to 16.521 for PD-CNN and 22.663 for ABT-DCNN. The significant improvement in MCC highlights the robustness of SLIA-ResNet50, ensuring better generalization and adaptability in medical imaging.

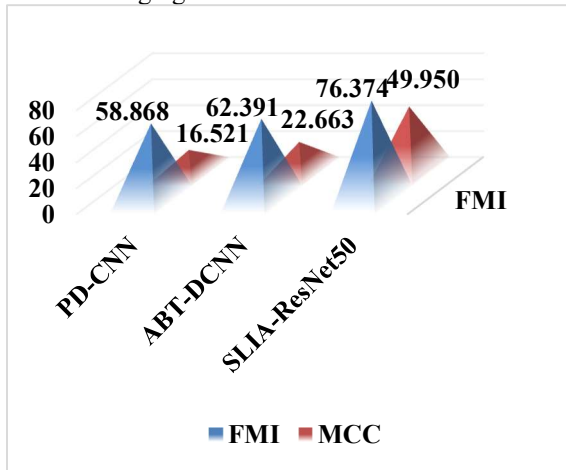


Fig 3. FMI and MCC

Fig 3. Illustrates the obtained results of the models under the parameter metric FMI and MCC. The results validate that integrating bio-inspired optimization enhances model efficiency, particularly in achieving higher classification accuracy and minimizing misclassification errors. The optimized hierarchical feature extraction and multi-scale integration techniques embedded in SLIA-ResNet50 contribute to its superior performance, reinforcing its effectiveness in MRI-based tumor classification.

Precision measures the proportion of correctly predicted positive instances among all predicted positives, indicating the model's ability to minimize false positives. Higher precision values demonstrate the model's efficiency in correctly classifying tumor regions while avoiding misclassifications. The results show that SLIA-ResNet50 achieves the highest precision at 72.416, significantly improving upon PD-CNN (53.771) and ABT-DCNN (57.274). The increased precision confirms the optimized feature extraction and real-time adaptability of SLIA-ResNet50, ensuring that false positive rates remain minimal.

Recall represents the ability of a model to identify all actual positive cases by minimizing false negatives. A higher recall value indicates that the model effectively detects tumor regions without missing critical abnormalities. SLIA-ResNet50 achieves the highest recall at 80.548, surpassing PD-CNN (64.447) and ABT-DCNN (67.966). The substantial improvement in recall highlights the role

of hierarchical feature integration and collaborative filtering layers, allowing SLIA-ResNet50 to capture complex patterns in MRI images with greater sensitivity.

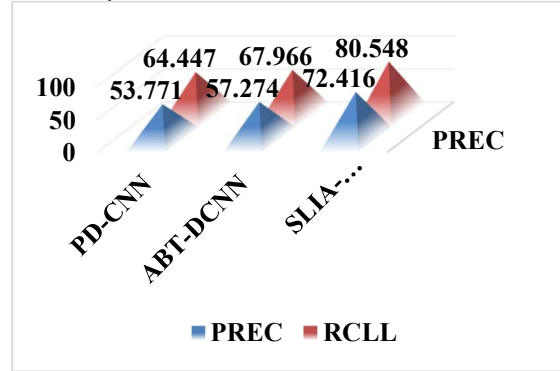


Fig 4. Precision and Recall

Fig 4. Illustrates the obtained results of the models under the parameter metric Precision and Recall. The results validate that bio-inspired optimization significantly enhances classification performance by improving both precision and recall. The superior balance between these metrics in SLIA-ResNet50 ensures higher diagnostic reliability, reducing both false positives and false negatives in MRI-based tumor classification. These findings establish the effectiveness of adaptive bio-inspired strategies in optimizing deep learning architectures for medical imaging applications.

SLIA-RN50 demonstrates superior performance than PD-CNN and ABT-DCNN because it generates substantially higher scores in classification accuracy as well as F-measure and recall measurements. The implementation of sea lion-based adaptive capabilities adds new energy-efficient learning methods with multi-scale feature processing features which improve performance in accuracy and convergence rate. Unlike PD-CNN's parallel structure that favors faster computation or ABT-DCNN's simplicity for lower-resource environments, SLIA-RN50 involves a more complex architecture requiring higher computational resources during training, which may limit its application in low-power clinical setups. While most existing models focus on static preprocessing and uniform feature selection, SLIA-RN50 introduces region-specific focus and dynamic adaptability—a biologically driven concept—marking a paradigm shift in tumor classification strategies. Despite its complex computational processing requirements this dynamic behavioral pattern provides possible avenues for evolving diagnostic models independently.

## 6. CONCLUSION

The Sea Lion Inspired Adaptive ResNet50 (SLIA-RN50) implements brain tumor classification through MRI data by integrating adaptive behavior models from sea lions into deep learning architecture. The proposed analysis delivers a special mix of biological intelligence mechanisms which includes hierarchical feature detection and region-based attention and information sharing algorithms and power-efficient processing technology. SLIA-RN50 operates differently from standard models because it changes its learning mechanisms to match the complexity of input data while providing better accuracy alongside precision and recall along with improved classification stability.

The innovative aspect combines real-time adaptation capabilities with nature-based decision strategies into multi-level processing systems to create a paradigm-shifting model named SLIA-RN50 for medical imaging deep learning. The proposed method tackles essential problems in present-day MRI-based tumor classification techniques which lead to classification mistakes and information reduction while demanding excessive computer processing. The clinical environment of modern times requires early and precise diagnosis so the proposed model offers an intelligent and scalable solution. Modern healthcare facilities can integrate SLIA-RN50 frameworks into computer-aided diagnosis systems because of their capability to handle complex inputs.

## REFERENCES

- [1]. B. Barati, M. Erfaninejad, and H. Khanbabaee, "Evaluation of effect of optimizers and loss functions on prediction accuracy of brain tumor type using a Light neural network," *Biomed Signal Process Control*, vol. 103, p. 107409, 2025, doi: <https://doi.org/10.1016/j.bspc.2024.107409>.
- [2]. K. N. Rao *et al.*, "An efficient brain tumor detection and classification using pre-trained convolutional neural network models," *Heliyon*, vol. 10, no. 17, p. e36773, 2024, doi: <https://doi.org/10.1016/j.heliyon.2024.e36773>.
- [3]. A. Bose and R. Garg, "Optimized CNN Using Manta-Ray Foraging Optimization for Brain Tumour Detection," *Procedia Comput Sci*, vol. 235, pp. 2187–2195, 2024, doi: <https://doi.org/10.1016/j.procs.2024.04.207>.
- [4]. G. D. Krishnamoorthy and K. Balasubramanian, "Multivariate technique for the prediction and classification of brain tumor using deep shallow network," *Appl Soft Comput*, vol. 164, p. 111962, 2024, doi: <https://doi.org/10.1016/j.asoc.2024.111962>.
- [5]. Md. N. Islam, Md. S. Azam, Md. S. Islam, M. H. Kanchan, A. H. M. S. Parvez, and Md. M. Islam, "An improved deep learning-based hybrid model with ensemble techniques for brain tumor detection from MRI image," *Inform Med Unlocked*, vol. 47, p. 101483, 2024, doi: <https://doi.org/10.1016/j.imu.2024.101483>.
- [6]. T. Saeed *et al.*, "Neuro-XAI: Explainable deep learning framework based on deeplabV3+ and bayesian optimization for segmentation and classification of brain tumor in MRI scans," *J Neurosci Methods*, vol. 410, p. 110247, 2024, doi: <https://doi.org/10.1016/j.jneumeth.2024.110247>.
- [7]. M. I. Nazir, A. Akter, M. A. Hussen Wadud, and M. A. Uddin, "Utilizing customized CNN for brain tumor prediction with explainable AI," *Heliyon*, vol. 10, no. 20, p. e38997, 2024, doi: <https://doi.org/10.1016/j.heliyon.2024.e38997>.
- [8]. A. Malik and G. G. Devarajan, "Integrated Brain Tumor Detection: PSO-Guided Segmentation with U-Net and CNN Classification," *Procedia Comput Sci*, vol. 235, pp. 3447–3457, 2024, doi: <https://doi.org/10.1016/j.procs.2024.04.325>.
- [9]. O. Bouguerra, B. Attallah, and Y. Brik, "MRI-based brain tumor ensemble classification using two stage score level fusion and CNN models," *Egyptian Informatics Journal*, vol. 28, p. 100565, 2024, doi: <https://doi.org/10.1016/j.eij.2024.100565>.
- [10]. M. R. Shoaib *et al.*, "Improving Brain Tumor Classification: An Approach Integrating Pre-Trained CNN Models and Machine Learning Algorithms," *Heliyon*, p. e33471, 2024, doi: <https://doi.org/10.1016/j.heliyon.2024.e33471>.
- [11]. T. Rahman and M. S. Islam, "MRI brain tumor detection and classification using parallel deep convolutional neural networks," *Measurement: Sensors*, vol. 26, p. 100694, 2023, doi: <https://doi.org/10.1016/j.measen.2023.100694>.

- [12]. J. C.P. and S. P. A. L., "PyQDCNN: Pyramid QDCNNNet for multi-level brain tumor classification using MRI image," *Biomed Signal Process Control*, vol. 100, p. 107042, 2025, doi: <https://doi.org/10.1016/j.bspc.2024.107042>.
- [13]. M. Arumugam, A. Thiagarajan, L. Adhi, and S. Alagar, "Crossover smell agent optimized multilayer perceptron for precise brain tumor classification on MRI images," *Expert Syst Appl*, vol. 238, p. 121453, 2024, doi: <https://doi.org/10.1016/j.eswa.2023.121453>.
- [14]. P. Kanchanamala, R. K.G., and M. B. J. Ananth, "Optimization-enabled hybrid deep learning for brain tumor detection and classification from MRI," *Biomed Signal Process Control*, vol. 84, p. 104955, 2023, doi: <https://doi.org/10.1016/j.bspc.2023.104955>.
- [15]. S. Jaga and K. Rama Devi, "Brain tumor classification utilizing Triple Memristor Hopfield Neural Network optimized with Northern Goshawk Optimization for MRI image," *Biomed Signal Process Control*, vol. 95, p. 106450, 2024, doi: <https://doi.org/10.1016/j.bspc.2024.106450>.
- [16]. A. K. Sahoo, P. Parida, M. K. Panda, K. Muralibabu, and A. S. Mohanty, "MultiTumor Analyzer (MTA-20-55): A network for efficient classification of detected brain tumors from MRI images," *Biocybern Biomed Eng*, vol. 44, no. 3, pp. 617–634, 2024, doi: <https://doi.org/10.1016/j.bbe.2024.06.003>.
- [17]. A. Rath, B. S. P. Mishra, and D. K. Bagal, "ResNet50-based Deep Learning model for accurate brain tumor detection in MRI scans," *Next Research*, vol. 2, no. 1, p. 100104, 2025, doi: <https://doi.org/10.1016/j.nexres.2024.100104>.
- [18]. M. S. Mithun and S. Joseph Jawhar, "Detection and classification on MRI images of brain tumor using YOLO NAS deep learning model," *J Radiat Res Appl Sci*, vol. 17, no. 4, p. 101113, 2024, doi: <https://doi.org/10.1016/j.jrras.2024.101113>.
- [19]. L. Mani, S. Arumugam, and R. Jaganathan, "Performance Enhancement of Wireless Sensor Network Using Feisty Particle Swarm Optimization Protocol," *ACM International Conference Proceeding Series*, pp. 1–5, Dec. 2022, doi: [10.1145/3590837.3590907](https://doi.org/10.1145/3590837.3590907).
- [20]. R. Karthikeyan and R. Vadivel, "Boosted Mutated Corona Virus Optimization Routing Protocol (BMCVORP) for Reliable Data Transmission with Efficient Energy Utilization," *Wirel Pers Commun*, vol. 135, no. 4, pp. 2281–2301, 2024, doi: [10.1007/s11277-024-11155-7](https://doi.org/10.1007/s11277-024-11155-7).
- [21]. T. Zhou, "Modality-level cross-connection and attentional feature fusion based deep neural network for multi-modal brain tumor segmentation," *Biomed Signal Process Control*, vol. 81, p. 104524, 2023, doi: <https://doi.org/10.1016/j.bspc.2022.104524>.
- [22]. Md. A. Rahman *et al.*, "GliomaCNN: An Effective Lightweight CNN Model in Assessment of Classifying Brain Tumor from Magnetic Resonance Images Using Explainable AI," *CMES - Computer Modeling in Engineering and Sciences*, vol. 140, no. 3, pp. 2425–2448, 2024, doi: <https://doi.org/10.32604/cmcs.2024.050760>.
- [23]. R. Appiah *et al.*, "Brain tumor detection using proper orthogonal decomposition integrated with deep learning networks," *Comput Methods Programs Biomed*, vol. 250, p. 108167, 2024, doi: <https://doi.org/10.1016/j.cmpb.2024.108167>.
- [24]. T. Singh, R. R. Nair, T. Babu, A. Wagh, A. Bhosalea, and P. Duraisamy, "BrainNet: A Deep Learning Approach for Brain Tumor Classification," *Procedia Comput Sci*, vol. 235, pp. 3283–3292, 2024, doi: <https://doi.org/10.1016/j.procs.2024.04.310>.
- [25]. S. Deepak and P. M. Ameer, "Brain tumor categorization from imbalanced MRI dataset using weighted loss and deep feature fusion," *Neurocomputing*, vol. 520, pp. 94–102, 2023, doi: <https://doi.org/10.1016/j.neucom.2022.11.039>.
- [26]. V. Vinay Kumar and P. Grace Kanmani Prince, "Deep belief network Assisted quadratic logit boost classifier for brain tumor detection using MR images," *Biomed Signal Process Control*, vol. 81, p. 104415, 2023, doi: <https://doi.org/10.1016/j.bspc.2022.104415>.
- [27]. P. T. Adinata, M. D. Chrispradipta, Meiliana, and A. Y. Zakiyyah, "An improved brain tumor detection model using ensemble boosting," *Procedia Comput Sci*, vol. 245, pp. 689–699, 2024, doi: <https://doi.org/10.1016/j.procs.2024.10.295>.
- [28]. S. P. Jakhar, A. Nandal, A. Dhaka, A. Alhudhaif, and K. Polat, "Brain tumor detection with multi-scale fractal feature network and fractal residual learning," *Appl Soft Comput*, vol. 153, p. 111284, 2024, doi: <https://doi.org/10.1016/j.asoc.2024.111284>.
- [29]. M. G. Abbas Malik, A. Saeed, K. Shehzad, and M. Iqbal, "DEF-SwinE2NET: Dual enhanced

- features guided with multi-model fusion for brain tumor classification using preprocessing optimization,” *Biomed Signal Process Control*, vol. 100, p. 107079, 2025, doi: <https://doi.org/10.1016/j.bspc.2024.107079>.
- [30]. B. Sreenivasa Reddy and A. Sathish, “A Multiscale Atrous Convolution-based Adaptive ResUNet3 + with Attention-based ensemble convolution networks for brain tumour segmentation and classification using heuristic improvement,” *Biomed Signal Process Control*, vol. 91, p. 105900, 2024, doi: <https://doi.org/10.1016/j.bspc.2023.105900>.
- [31]. I. S. Al Naimi, S. A. A. S. Junid, M. Imran Ahmad, and K. S. Manic, “Automatic Finding of Brain-Tumour Group Using CNN Segmentation and Moth-Flame-Algorithm, Selected Deep and Handcrafted Features,” *Computers, Materials and Continua*, vol. 79, no. 2, pp. 2585–2608, 2024, doi: <https://doi.org/10.32604/cm.2024.046461>.
- [32]. E. J. Alwadee, X. Sun, Y. Qin, and F. C. Langbein, “LATUP-Net: A lightweight 3D attention U-Net with parallel convolutions for brain tumor segmentation,” *Comput Biol Med*, vol. 184, p. 109353, 2025, doi: <https://doi.org/10.1016/j.compbiomed.2024.109353>.
- [33]. A. M. Dikande Simo, A. Tchagna Kouanou, V. Monthe, M. Kameni Nana, and B. Moffo Lonla, “Introducing a deep learning method for brain tumor classification using MRI data towards better performance,” *Inform Med Unlocked*, vol. 44, p. 101423, 2024, doi: <https://doi.org/10.1016/j.imu.2023.101423>.
- [34]. T. Zhou, “Multi-modal brain tumor segmentation via disentangled representation learning and region-aware contrastive learning,” *Pattern Recognit*, vol. 149, p. 110282, 2024, doi: <https://doi.org/10.1016/j.patcog.2024.110282>.
- [35]. A. Hossain, R. Islam, M. T. Islam, P. Kirawanich, and M. S. Soliman, “FT-FEDTL: A fine-tuned feature-extracted deep transfer learning model for multi-class microwave-based brain tumor classification,” *Comput Biol Med*, vol. 183, p. 109316, 2024, doi: <https://doi.org/10.1016/j.compbiomed.2024.109316>.
- [36]. T. Rahman and M. S. Islam, “MRI brain tumor detection and classification using parallel deep convolutional neural networks,” *Measurement: Sensors*, vol. 26, p. 100694, 2023, doi: <https://doi.org/10.1016/j.measen.2023.100694>.
- [37]. Md. S. I. Khan *et al.*, “Accurate brain tumor detection using deep convolutional neural network,” *Comput Struct Biotechnol J*, vol. 20, pp. 4733–4745, 2022, doi: <https://doi.org/10.1016/j.csbj.2022.08.039>.
- [38]. B. Suchitra, J. Ramkumar, and R. Karthikeyan, “Frog Leap Inspired Optimization-Based Extreme Learning Machine For Accurate Classification Of Latent Autoimmune Diabetes In Adults (LADA),” *J. Theor. Appl. Inf. Technol.*, vol. 103, no. 2, pp. 472–494, 2025.
- [39]. J. Ramkumar, V. Valarmathi, and R. Karthikeyan, “Optimizing Quality of Service and Energy Efficiency in Hazardous Drone Ad-Hoc Networks (DANET) Using Kingfisher Routing Protocol (KRP),” *Int. J. Eng. Trends Technol.*, vol. 73, no. 1, pp. 410–430, 2025, doi: [10.14445/22315381/IJETT-V73I1P135](https://doi.org/10.14445/22315381/IJETT-V73I1P135).
- [40]. J. Ramkumar, B. Varun, V. Valarmathi, D. R. Medhunhashini, and R. Karthikeyan, “Jaguar-Based Routing Protocol (JRP) For Improved Reliability And Reduced Packet Loss In Drone Ad-Hoc Networks (DANET),” *J. Theor. Appl. Inf. Technol.*, vol. 103, no. 2, pp. 696–713, 2025.
- [41]. [4] R. Jaganathan, S. Mehta, and R. Krishan, “Preface,” *Bio-Inspired Intell. Smart Decis.*, pp. xix–xx, 2024.
- [42]. J. Ramkumar and R. Vadivel, “Multi-Adaptive Routing Protocol for Internet of Things based Ad-hoc Networks,” *Wirel. Pers. Commun.*, vol. 120, no. 2, pp. 887–909, Apr. 2021, doi: [10.1007/s11277-021-08495-z](https://doi.org/10.1007/s11277-021-08495-z).
- [43]. A. Senthilkumar, J. Ramkumar, M. Lingaraj, D. Jayaraj, and B. Sureshkumar, “Minimizing Energy Consumption in Vehicular Sensor Networks Using Relentless Particle Swarm Optimization Routing,” *Int. J. Comput. Networks Appl.*, vol. 10, no. 2, pp. 217–230, 2023, doi: [10.22247/ijcna/2023/220737](https://doi.org/10.22247/ijcna/2023/220737).
- [44]. S. P. Priyadarshini and J. Ramkumar, “Mappings Of Plithogenic Cubic Sets,” *Neutrosophic Sets Syst.*, vol. 79, pp. 669–685, 2025, doi: [10.5281/zenodo.14607210](https://doi.org/10.5281/zenodo.14607210).
- [45]. J. Ramkumar and R. Vadivel, “Improved Wolf prey inspired protocol for routing in cognitive radio Ad Hoc networks,” *Int. J. Comput. Networks Appl.*, vol. 7, no. 5, pp. 126–136, 2020, doi: [10.22247/ijcna/2020/202977](https://doi.org/10.22247/ijcna/2020/202977).
- [46]. R. Jaganathan and R. Vadivel, “Intelligent Fish Swarm Inspired Protocol (IFSIP) for Dynamic Ideal Routing in Cognitive Radio Ad-Hoc Networks,” *Int. J. Comput. Digit. Syst.*, vol.

- 10, no. 1, pp. 1063–1074, 2021, doi: 10.12785/ijcds/100196.
- [47]. J. Ramkumar and R. Vadivel, “CSIP—cuckoo search inspired protocol for routing in cognitive radio ad hoc networks,” in *Advances in Intelligent Systems and Computing*, Springer Verlag, 2017, pp. 145–153. doi: 10.1007/978-981-10-3874-7\_14.
- [48]. S. P. Geetha, N. M. S. Sundari, J. Ramkumar, and R. Karthikeyan, “Energy Efficient Routing In Quantum Flying Ad Hoc Network (Q-Fanet) Using Mamdani Fuzzy Inference Enhanced Dijkstra’s Algorithm (MFI-EDA),” *J. Theor. Appl. Inf. Technol.*, vol. 102, no. 9, pp. 3708–3724, 2024.
- [49]. M. P. Swapna, J. Ramkumar, and R. Karthikeyan, “Energy-Aware Reliable Routing with Blockchain Security for Heterogeneous Wireless Sensor Networks,” in *Lecture Notes in Networks and Systems*, V. Goar, M. Kuri, R. Kumar, and T. Senjyu, Eds., Springer Science and Business Media Deutschland GmbH, 2025, pp. 713–723. doi: 10.1007/978-981-97-6106-7\_43.
- [50]. J. Ramkumar, K. S. Jeen Marseline, and D. R. Medhunhashini, “Relentless Firefly Optimization-Based Routing Protocol (RFORP) for Securing Fintech Data in IoT-Based Ad-Hoc Networks,” *Int. J. Comput. Networks Appl.*, vol. 10, no. 4, pp. 668–687, 2023, doi: 10.22247/ijcna/2023/223319.
- [51]. K. S. J. Marseline, J. Ramkumar, and D. R. Medhunhashini, “Sophisticated Kalman Filtering-Based Neural Network for Analyzing Sentiments in Online Courses,” in *Smart Innovation, Systems and Technologies*, A. K. Somani, A. Mundra, R. K. Gupta, S. Bhattacharya, and A. P. Mazumdar, Eds., Springer Science and Business Media Deutschland GmbH, 2024, pp. 345–358. doi: 10.1007/978-981-97-3690-4\_26.
- [52]. J. Ramkumar and R. Vadivel, “Whale optimization routing protocol for minimizing energy consumption in cognitive radio wireless sensor network,” *Int. J. Comput. Networks Appl.*, vol. 8, no. 4, pp. 455–464, 2021, doi: 10.22247/ijcna/2021/209711.
- [53]. M. P. Swapna and J. Ramkumar, “Multiple Memory Image Instances Stratagem to Detect Fileless Malware,” in *Communications in Computer and Information Science*, S. Rajagopal, K. Popat, D. Meva, and S. Bajaja, Eds., Springer Science and Business Media Deutschland GmbH, 2024, pp. 131–140. doi: 10.1007/978-3-031-59100-6\_11.
- [54]. D. Jayaraj, J. Ramkumar, M. Lingaraj, and B. Sureshkumar, “AFSORP: Adaptive Fish Swarm Optimization-Based Routing Protocol for Mobility Enabled Wireless Sensor Network,” *Int. J. Comput. Networks Appl.*, vol. 10, no. 1, pp. 119–129, 2023, doi: 10.22247/ijcna/2023/218516.
- [55]. M. Lingaraj, T. N. Sugumar, C. S. Felix, and J. Ramkumar, “Query aware routing protocol for mobility enabled wireless sensor network,” *Int. J. Comput. Networks Appl.*, vol. 8, no. 3, pp. 258–267, 2021, doi: 10.22247/ijcna/2021/209192.
- [56]. R. Jaganathan, S. Mehta, and R. Krishan, *Bio-Inspired intelligence for smart decision-making*. IGI Global, 2024. doi: 10.4018/9798369352762.
- [57]. R. Vadivel and J. Ramkumar, “QoS-enabled improved cuckoo search-inspired protocol (ICSIP) for IoT-based healthcare applications,” in *Incorporating the Internet of Things in Healthcare Applications and Wearable Devices*, IGI Global, 2019, pp. 109–121. doi: 10.4018/978-1-7998-1090-2.ch006.
- [58]. J. Ramkumar, R. Karthikeyan, and M. Lingaraj, “Optimizing IoT-Based Quantum Wireless Sensor Networks Using NM-TEEN Fusion of Energy Efficiency and Systematic Governance,” in *Lecture Notes in Electrical Engineering*, V. Shrivastava, J. C. Bansal, and B. K. Panigrahi, Eds., Springer Science and Business Media Deutschland GmbH, 2025, pp. 141–153. doi: 10.1007/978-981-97-6710-6\_12.
- [59]. J. Ramkumar, R. Karthikeyan, and V. Valarmathi, “Alpine Swift Routing Protocol (ASRP) for Strategic Adaptive Connectivity Enhancement and Boosted Quality of Service in Drone Ad Hoc Network (DANET),” *Int. J. Comput. Networks Appl.*, vol. 11, no. 5, pp. 726–748, 2024, doi: 10.22247/ijcna/2024/45.
- [60]. P. Menakadevi and J. Ramkumar, “Robust Optimization Based Extreme Learning Machine for Sentiment Analysis in Big Data,” in *2022 International Conference on Advanced Computing Technologies and Applications*, ICACTA 2022, Institute of Electrical and Electronics Engineers Inc., 2022. doi: 10.1109/ICACTA54488.2022.9753203.
- [61]. J. Ramkumar, A. Senthilkumar, M. Lingaraj, R. Karthikeyan, and L. Santhi, “Optimal Approach For Minimizing Delays In Iot-Based Quantum Wireless Sensor Networks Using Nm-Leach Routing Protocol,” *J. Theor. Appl.*

- Inf. Technol., vol. 102, no. 3, pp. 1099–1111, 2024.
- [62]. J. Ramkumar and R. Vadivel, “Improved frog leap inspired protocol (IFLIP) – for routing in cognitive radio ad hoc networks (CRAHN),” *World J. Eng.*, vol. 15, no. 2, pp. 306–311, 2018, doi: 10.1108/WJE-08-2017-0260.
- [63]. R. Jaganathan, S. Mehta, and R. Krishan, *Intelligent Decision Making Through Bio-Inspired Optimization*. IGI Global, 2024. doi: 10.4018/979-8-3693-2073-0.
- [64]. R. Jaganathan and V. Ramasamy, “Performance modeling of bio-inspired routing protocols in Cognitive Radio Ad Hoc Network to reduce end-to-end delay,” *Int. J. Intell. Eng. Syst.*, vol. 12, no. 1, pp. 221–231, 2019, doi: 10.22266/IJIES2019.0228.22.
- [65]. R. Karthikeyan and R. Vadivel, “Boosted Mutated Corona Virus Optimization Routing Protocol (BMCVORP) for Reliable Data Transmission with Efficient Energy Utilization,” *Wirel. Pers. Commun.*, vol. 135, no. 4, pp. 2281–2301, 2024, doi: 10.1007/s11277-024-11155-7.
- [66]. R. Karthikeyan and R. Vadivel, “Proficient Dazzling Crow Optimization Routing Protocol (PDCORP) for Effective Energy Administration in Wireless Sensor Networks,” in *IEEE International Conference on Electrical, Electronics, Communication and Computers, ELEXCOM 2023*, 2023, pp. 1–6. doi: 10.1109/ELEXCOM58812.2023.10370559.
- [67]. N. K. Ojha, A. Pandita, and J. Ramkumar, “Cyber security challenges and dark side of AI: Review and current status,” in *Demystifying the Dark Side of AI in Business*, 2024, pp. 117–137. doi: 10.4018/979-8-3693-0724-3.ch007.
- [68]. J. Ramkumar, S. S. Dinakaran, M. Lingaraj, S. Boopalan, and B. Narasimhan, “IoT-Based Kalman Filtering and Particle Swarm Optimization for Detecting Skin Lesion,” in *Lecture Notes in Electrical Engineering*, K. Murari, N. Prasad Padhy, and S. Kamalasan, Eds., Singapore: Springer Nature Singapore, 2023, pp. 17–27. doi: 10.1007/978-981-19-8353-5\_2.
- [69]. J. Ramkumar, C. Kumuthini, B. Narasimhan, and S. Boopalan, “Energy Consumption Minimization in Cognitive Radio Mobile Ad-Hoc Networks using Enriched Ad-hoc On-demand Distance Vector Protocol,” in *2022 International Conference on Advanced Computing Technologies and Applications*, ICACTA 2022, 2022. doi: 10.1109/ICACTA54488.2022.9752899.
- [70]. J. Ramkumar, R. Vadivel, and B. Narasimhan, “Constrained Cuckoo Search Optimization Based Protocol for Routing in Cloud Network,” *Int. J. Comput. Networks Appl.*, vol. 8, no. 6, pp. 795–803, 2021, doi: 10.22247/ijena/2021/210727.